Title

Integrin mechanosensing relies on a pivot-clip mechanism to reinforce cell adhesion.

Journal

Biophysical Journal, 123(16)

Authors

Montes, Andre

Barroso, Anahi

Wang, Wei

et al.

Publication Date

2024-08-20

DOI

10.1016/j.bpj.2024.06.008

Peer reviewed

Biophysical Journal
Article

Biophysical Society

Integrin mechanosensing relies on a pivot-clip mechanism to reinforce cell adhesion

Andre R. Montes,[1] Anahi Barroso,[1] Wei Wang,[2,3] Grace D. O'Connell,[3] Adrian B. Tepole,[4,*] and Mohammad R. K. Mofrad[1,5,*]

[1]Molecular Cell Biomechanics Laboratory, Departments of Bioengineering and Mechanical Engineering, University of California, Berkeley, Berkeley, California; [2]Berkeley City College, Berkeley, California; [3]Berkeley Biomechanics Laboratory, Department of Mechanical Engineering, University of California, Berkeley, Berkeley, California; [4]Tepole Mechanics and Mechanobiology Laboratory, School of Mechanical Engineering, Purdue University, West Lafayette, Indiana; and [5]Molecular Biophysics and Integrative Bioimaging Division, Lawrence Berkeley National Lab, Berkeley, California

ABSTRACT Cells intricately sense mechanical forces from their surroundings, driving biophysical and biochemical activities. This mechanosensing phenomenon occurs at the cell-matrix interface, where mechanical forces resulting from cellular motion, such as migration or matrix stretching, are exchanged through surface receptors, primarily integrins, and their corresponding matrix ligands. A pivotal player in this interaction is the $\alpha_5\beta_1$ integrin and fibronectin (FN) bond, known for its role in establishing cell adhesion sites for migration. However, upregulation of the $\alpha_5\beta_1$-FN bond is associated with uncontrolled cell metastasis. This bond operates through catch bond dynamics, wherein the bond lifetime paradoxically increases with greater force. The mechanism sustaining the characteristic catch bond dynamics of $\alpha_5\beta_1$-FN remains unclear. Leveraging molecular dynamics simulations, our approach unveils a pivot-clip mechanism. Two key binding sites on FN, namely the synergy site and the RGD (Arg-Gly-Asp) motif, act as active points for structural changes in $\alpha_5\beta_1$ integrin. Conformational adaptations at these sites are induced by a series of hydrogen bond formations and breaks at the synergy site. We disrupt these adaptations through a double mutation on FN, known to reduce cell adhesion. A whole-cell finite-element model is employed to elucidate how the synergy site may promote dynamic $\alpha_5\beta_1$-FN binding, resisting cell contraction. In summary, our study integrates molecular- and cellular-level modeling to propose that FN's synergy site reinforces cell adhesion through enhanced binding dynamics and a mechanosensitive pivot-clip mechanism. This work sheds light on the interplay between mechanical forces and cell-matrix interactions, contributing to our understanding of cellular behaviors in physiological and pathological contexts.

SIGNIFICANCE $\alpha_5\beta_1$ integrin serves as a mediator of cell-matrix adhesion and has garnered attention as a target for impeding cancer metastasis. Despite its importance, the mechanism underlying the formation of a catch bond between $\alpha_5\beta_1$ integrin and its primary ligand, fibronectin, has remained elusive. Our study aims to address this gap by proposing a pivot-clip mechanism. This mechanism elucidates how $\alpha_5\beta_1$ integrin and fibronectin collaboratively reinforce cell adhesion through conformational changes induced by the dynamic interaction of a key binding motif known as the synergy site.

INTRODUCTION

Adhesion bonds enable cells to interact dynamically with their surrounding environment, orchestrating the regulation of essential cellular processes such as proliferation, differentiation, and apoptosis (1–5). Integrins are transmembrane, heterodimeric proteins that play an important role in cell adhesion by tethering the inside and outside of the cell via binding partners in the extracellular matrix (ECM) (6). $\alpha_5\beta_1$ integrin is one of 24 integrin heterodimers present in mammals (4) and mediates cell-tissue homeostasis by binding to its primary ligand, fibronectin (FN) (7,8). $\alpha_5\beta_1$ and FN are linked together at the RGD (Arg-Gly-Asp) motif and stabilized by the eight-amino-acid-long DRVPHSRN synergy site on FN (9), allowing extracellular and cytoplasmic forces to be transmitted across the cell membrane. The accumulation of $\alpha_5\beta_1$-FN bonds form the basis for nascent cell adhesion and cell motion. Beyond $\alpha_5\beta_1$-FN's role in maintaining cell-tissue homeostasis, it has been implicated as a potential therapeutic target for cancer (10–12). For example, dysfunctional and overexpressed integrin bonds are markers of uninhibited cancer cell migration

Submitted December 13, 2023, and accepted for publication June 7, 2024.

*Correspondence: abuganza@purdue.edu or mofrad@berkeley.edu

Editor: Frauke Graeter.

https://doi.org/10.1016/j.bpj.2024.06.008

(13,14). As such, numerous antagonists have been developed to attenuate integrin bonds, aiming to impede the invasion of multiple cancer cell types. Despite considerable efforts, these antagonists have faced challenges, demonstrating limited success in effectively preventing cancer cell invasion (15,16). Therefore, a better understanding of the biophysical nature of the $\alpha_5\beta_1$-FN bond is needed to reveal mechanisms that can be exploited to target metastasis.

$\alpha_5\beta_1$ integrin creates a catch bond with FN (9,17,18), which is a type of bond that increases in lifetime with greater applied force. The $\alpha_5\beta_1$-FN catch bond allows for strong adhesion at the leading edge of a migrating cell and a steady release of the bond at the cell's trailing end. Catch bonds have inspired development of synthetic catch bonds for manufacturing resilient materials (19–21). However, the mechanisms involved in the $\alpha_5\beta_1$-FN catch bond's ability to maintain its characteristic strength is unknown. Understanding the underlying mechanism of $\alpha_5\beta_1$-FN catch bond resilience could identify structural protein characteristics that can be targeted to arrest cancer cells through substrate or protein modifications. Moreover, structural dynamics that enable catch bond behavior may inspire development of resistant nanomaterials with self-strengthening properties.

Ideally, the $\alpha_5\beta_1$-FN catch bond could be imaged while an applied force is applied with a single-molecule testing setup (e.g., optical trap or magnetic tweezers). However, current atomic-resolution molecular imaging techniques, like cryo-EM and x-ray crystallography, require immobilizing the protein, making visualization of in situ structural changes of $\alpha_5\beta_1$-FN challenging. In light of these experimental limitations, molecular dynamics (MD) simulations have been used to visualize protein conformational changes over time (22,23).

Given $\alpha_5\beta_1$-FN's critical role in mechanosensing via its elusive catch bond dynamics, we used MD simulations to visualize the motion of $\alpha_5\beta_1$-FN when acted on by an external load. We introduce a "pivot-clip" mechanism to model the $\alpha_5\beta_1$-FN's catch bond-like behavior, where the RGD motif acts as a stable pivot for FN about β_1 integrin and the synergy site acts as a reinforcing clip connecting FN to α_5. Past experiments demonstrated that mutating the synergy site diminishes catch bond behavior and weakens whole-cell and single-molecule adhesion to $\alpha_5\beta_1$ (18,24). Even so, a lack of the synergy site does not significantly limit cell traction on a 2D substrate under minimal contractility (25). To explain how the synergy site may promote $\alpha_5\beta_1$-FN binding while maintaining cell traction, we developed a 2D finite element (FE) model of the adhesive interface. Based on our MD and FE models, we present a theory that the synergy site in FN reinforces cell adhesion via stronger binding affinity and a mechanosensitive pivot-clip mechanism.

MATERIALS AND METHODS

Steered MD simulations

Constant velocity, all-atom steered MD simulations of the ectoplasmic $\alpha_5\beta_1$-FN complex were run in GROMACS 2020.4 (26). The PDB: 7NWL crystal structure file of the $\alpha_5\beta_1$-FN complex with the TS2/16 Fv-clasp was downloaded from the protein data bank. The $\alpha_5\beta_1$ integrin head domain and the FN type III fragment 7–10 were isolated using PyMOL (27). We used MODELLER 10.4 (28) to impose a virtual R1374/9A double mutation, switching the arginine residues in positions 1374 and 1379 in FN to alanine (Fig. 1 *B*).

Wild-type and mutated structures were solvated in a TIP3P water box ($18 \times 45 \times 19$ nm) with 0.15 mM NaCl. Energy was minimized for 15k steps with the steepest gradient descent algorithm, followed by an equilibration sequence of a 1 ns NVT simulation at 310 K followed by a 10 ns NPT simulation at 1 bar and 310 K, as per physiological conditions. Equilibration was verified by ensuring that the RMSD of the fully unrestrained complexes (Fig. S1) were within 0.3 nm resolution of cryo-EM.

The K559 and E36 residues at the proximal ends of the integrin headpieces were then restrained. P1142 at the distal end of the FN fragment was pulled at 10 and 1 nm/ns using a 50 kJ/mol/nm spring with an umbrella potential for 3 and 20 ns, respectively. The steered MD simulations used a 2 fs time step. We visualized the crystal structures and MD simulation trajectories using Visual Molecular Dynamics (VMD) 1.9.4a (29). All parameters for the MD simulations are available in the supporting material (Table S1). The force and extension at $\alpha_5\beta_1$-FN's center-of-mass (COM) were derived directly from the output files from GROMACS. The extension was measured as the displacement of the $\alpha_5\beta_1$-FN's COM with respect to the first simulation frame. The radius of gyration of the α_5 and β_1 heads was measured using the built-in GROMACS function, gmx gyrate. Distances between key bonds at R1374 and R1379 were calculated by averaging the distance between atom pairs that could form hydrogen bonds using the VMD bond select and graph tool. We used a distance cutoff of 0.35 nm (3.5 Å) and donor-hydrogen-acceptor angle cutoff of 30 in VMD to detect hydrogen bonds.

Synergy site departure energy

To calculate the energy required for the synergy site to depart from α_5, we used in-house Python code to integrate the force and COM extension data from the beginning of the simulation to the time of the force peak just before the rapid increase in extension rate. Since the force-extension data are nonmonotonic, we first fitted a piece-wise linear function over the force-extension data before integrating with trapezoid rule.

Force distribution analysis

Time-resolved force distribution analysis was used to measure the punctual stresses based on the Coulombic interactions at all residues across all simulation time steps (30). The punctual stress is the absolute value of scalar pairwise forces exerted on each residue. Normally, stress would be in units of energy. However, the developers of punctual stress defined it as "force on a dimensionless point," which uses units of force (kJ/mol-nm). We opted to use this definition of punctual stress to remain consistent with past studies. Parameters for the time-resolved force distribution analysis are available in the supplementary material (Table S2).

Long-term NPT equilibration simulations

Longer-term stability of the $\alpha_5\beta_1$-FN complex after synergy site mutagenesis was tested with two 250 ns NPT simulations of $\alpha_5\beta_1$-FN9-10: one wild-type and one R1374/9A mutant. The PDB: 7NWL file was

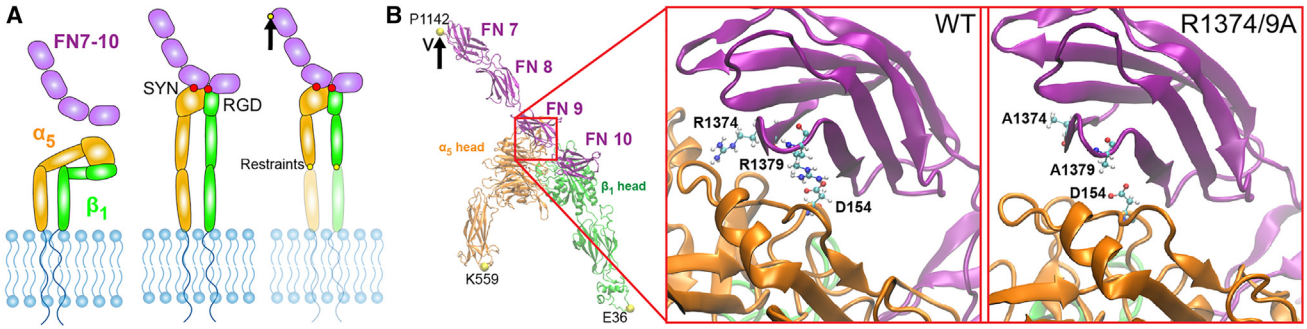

FIGURE 1 (*A*) Schematics of $\alpha_5\beta_1$ integrin in its bent-closed, inactive state with FN fragment 7–10 unbounded (*left*), extended-active state in complex with FN (*middle*), and under an applied load (*right*). (*B*) The cryo-EM structure of $\alpha_5\beta_1$-FN with the individual integrin heads and FN fragments labeled. The MD simulations applied a velocity to the P1142 residue while restraining K559 and E36. Zoomed-in region shows wild-type synergy site with R1374 and R1379 (*left*) and double mutated R1374/9A synergy site (*right*). D154 binds to R1379 and is shown as a reference. SYN, synergy site; RGD, Arg-Gly-Asp. To see this figure in color, go online.

truncated from $\alpha_5\beta_1$-FN7-10 to $\alpha_5\beta_1$-FN9-10. An R1374/9A double mutation was again induced in silico via MODELLER 10.4 (28). The system contained ≈1.3M atoms in a 15 × 30 × 30 nm box after solvation. NaCl concentration was kept at 0.15 mM. The 250 ns NPT simulation was preceded by a 15k step energy minimization and 1 ns NVT as described previously. Restraints (100 kJ/mol-nm^2) were placed on residues D603, E445, and D1328 (Fig. 4 *A*) in the *x* and *y* directions, representing the remaining structures of integrin and FN while limiting periodic box crossing. No other restraints were placed. We used GROMACS 2020.4 (26) to measure backbone RMSDs, nonbonded energies, axes of inertia, distances, and hydrogen bonds. Axes of inertia were used to calculate angles by taking the inverse cosine of the dot product of a unit vector pair. Measurements were tested for normality with the Kolmogorov-Smirnov test. Since all data were nonnormal, the wild-type and mutant trajectories were compared using the Wilcoxon signed rank test ($\alpha = 0.05$).

Extensional stiffness of α_5 and β_1 headpieces

Extensional stiffnesses of α_5 and β_1 headpieces were determined independently using 100 ns NPT simulations. The PDB: 7NWL file was isolated to either the α_5 head (≈438 K atoms in a 16.5 × 16.5 × 16.5 nm box post solvation) or β_1 head (≈463 K atoms in a 16.8 × 16.8 × 16.8 nm box post solvation). Again, energy minimization for 15k steps and a 1 ns NVT as previously described were run in GROMACS before the 100 ns NPT simulation. Extensional stiffness, *k*, for each molecule was calculated using:

$$k = \frac{k_B T}{< (L(t) - < L(t) >_{\Delta t})^2 >_{\Delta t}}, \qquad \text{(Equation 1)}$$

where $k_B T$ is Boltzmann's constant, $T = 310$ K, $L(t)$ is the length of the reaction coordinate at time, *t*, and $< >$ denotes the time average (31). For α_5, the COM distance between D154 (synergy site binding residue) and D603 (connects to lower integrin legs) in α_5 was chosen as the length of the reaction coordinate. Similarly for β_1, the Metal-Ion Dependent Adhesion Site (MIDAS) (binds to RGD) and E445 (connects to lower integrin legs) were chosen. After the system had equilibrated, we used the latter 50 ns for the extensional stiffness calculation. For each molecule, the distance data were divided into five 10 ns blocks. Distances were saved every 10 ps during the simulation, resulting in 1000 data points per block to calculate five *k* values per head. A Wilcoxon signed-rank test compared the means of the extensional stiffnesses of α_5 and β_1. The angle between the propeller and thigh in α_5 was measured as described previously.

Whole-cell FE model

We used a whole-cell FE model to calculate the $\alpha_5\beta_1$-FN concentration and force in a wild-type and mutant cell. We have previously modeled the cell-substrate interface using a whole-cell FE model; we refer the reader to that publication for the full set of model Equation 23. In this work, we introduced key changes to the catch bond model. We modeled the cell as a 2D elastic disk with neo-Hookean constitutive material properties on a rigid substrate,

$$\boldsymbol{\sigma}_c^{pas} = \mu_c \mathbf{b_c} - p_c \mathbf{I}, \qquad \text{(Equation 2)}$$

where σ_c^{pas} is the passive cell stress. The cell shear modulus is, $\mu_c = 1$ kPa (32,33). The deformation was characterized by the left Cauchy-Green tensor $\mathbf{b_c}$. The pressure p_c was computed from plane stress boundary conditions.

An isotropic active stress field was applied inside the cell to model cell contractility,

$$\boldsymbol{\sigma}_c^{act} = t_{myo} \mathbf{I}, \qquad \text{(Equation 3)}$$

where $\boldsymbol{\sigma}_c^{act}$ is the active cell stress due to an actomyosin traction, t_{myo} in Pa (33,34):

$$t_{myo} = \begin{cases} 100\ [\text{Pa/s}]\ t\ [\text{s}] & 0 < t < 2\ [\text{s}] \\ 200\ [\text{Pa}] & 2 \le t \le 30\ [\text{s}] \end{cases} \qquad \text{(Equation 4)}$$

where *t* is the simulation time.

We used an existing catch bond model of adhesion to calculate the force-dependent concentration of $\alpha_5\beta_1$-FN bonds per node in the FE mesh (35–38). The catch model assumed that the $\alpha_5\beta_1$-FN complexes behave as parallel springs that connect and disconnect to the substrate based on an association constant, K_{on}, and on a force-dependent dissociation constant, K_{off}, respectively.

$$K_{off} = K_a e^{\frac{f_{int}}{F_a}} + K_b e^{-\frac{f_{int}}{F_b}}, \qquad \text{(Equation 5)}$$

where K_a, F_a, K_b, and F_b are fitted parameters (Table S3) adapted from Bidone et al. (38) and Takagi et al. (39). f_{int} is the magnitude of the force per $\alpha_5\beta_1$-FN bond. The force vector per bond, ($\mathbf{f_{int}}$), is computed via the $\alpha_5\beta_1$-FN spring constant $k_{int} = 0.5$ pN/nm (17) and the spring extension vector $\mathbf{u_{int}}$:

$$\mathbf{f_{int}} = k_{int} \mathbf{u_{int}}. \qquad \text{(Equation 6)}$$

The force per node, $\mathbf{f}_{i,node}$ is related to the dimensionless concentration of $\alpha_5\beta_1$-FN bonds *C* with respect to the maximum bond density $\rho_{i,max} = 100\ \mu\text{m}^2$ (40), and the local adhesion area *A* at that node,

$$\mathbf{f}_{i,node} = C\rho_{i_{max}} A\mathbf{f}_{\mathbf{int}}\,. \qquad \text{(Equation 7)}$$

At any node, i, given the previous value of the bond concentration, C, the updated bond concentration $C_{t+\Delta t}$ at each progressive time step is

$$C_{t+\Delta t} = C\left(1 - K_{off}\Delta t\right) + K_{on}\Delta t(1 - C)\,. \qquad \text{(Equation 8)}$$

Note that the updated Eq. 8 is based on treating the bond kinetics in the limit of an ordinary differential equation discretized in time with an explicit Euler scheme.

The internal force balance for the cell includes the elastic cell deformation ($\sigma_{\mathbf{c}}^{\mathbf{pas}}$) and the active cell contractile stress ($\sigma_{\mathbf{c}}^{\mathbf{act}}$):

$$\nabla \cdot \boldsymbol{\sigma_c} + \mathbf{B} = \rho_c \mathbf{a}_c, \qquad \text{(Equation 9)}$$

in which $\boldsymbol{\sigma_c} = \boldsymbol{\sigma_c^{pas}} + \boldsymbol{\sigma_c^{act}}$ is the total cell stress, $\mathbf{B}$ is the total body force on the cell, $\rho_c = 1000\,\mathrm{kg/m^3}$ is the cell density (41) and $\mathbf{a}_c$ is the cell acceleration.

The strong form of the elastodynamic Eq. 9 has boundary conditions of the form $\boldsymbol{\sigma}\cdot\mathbf{n} = \mathbf{t}$ on boundary Γ_c, which includes the external forces on the circumference. Assuming 2D plane stress, the body forces on the cell arise from $\alpha_5\beta_1$-FN bond forces and viscous drag forces. The internal forces were computed through the weak form. In brief, we multiplied Eq. 9 by test function, ν, integrated over a domain Ω_c of thickness 1 μm, and applied divergence theorem to get the following weak form for the cell.

$$-\int_{\Omega_c} \boldsymbol{\sigma_c} : \delta\mathbf{d_c}\, d\Omega_c + \int_{\Gamma_c} \mathbf{t_c}\cdot\boldsymbol{\nu}\, dA_c + \int_{\Omega} \boldsymbol{\nu}\cdot\mathbf{B} = -\mathbf{R_c} + \mathbf{f_{circ}} + \mathbf{f_{body}} = \int_{\Omega_c} \rho\mathbf{a_c}\cdot\boldsymbol{\nu}\, d\Omega_c, \qquad \text{(Equation 10)}$$

The $\delta\mathbf{d_c}$ is the variation of the symmetric velocity gradient, i.e., virtual work by moving each node by an independent variation ν. $\mathbf{R_c}$ is the residual (internal forces) and the external force acting at a node of the cell mesh is composed of the forces on the circumference, $\mathbf{f_{circ}}$ and the forces on the body, $\mathbf{f_{body}}$:

$$\mathbf{f_{circ}} = \mathbf{f}_\kappa + \mathbf{f}_{ac} + \mathbf{f}_A, \qquad \text{(Equation 11)}$$

$$\mathbf{f_{body}} = \mathbf{f}_{i,node} + \mathbf{f}_d, \qquad \text{(Equation 12)}$$

where $\mathbf{f}_{i,node}$ is the force due to $\alpha_5\beta_1$-FN at each node, $\mathbf{f}_d$ is viscous drag, $\mathbf{f}_\kappa$ is curvature regularization, $\mathbf{f}_{ac}$ is a random fluctuation at the cell boundary from actin polymerization, and $\mathbf{f}_A$ is an area penalty to counteract cell contractility.

The mesh was updated by a dynamic explicit mesh generator, El Topo (42), during the simulation run. The explicit midpoint rule was used for time integration of the second-order system of equations to update nodal velocities and positions. The whole-cell FE simulation ran with a time step of 50 μs over the course of an assigned time of $t_{sim} = 30$ s. There were a total of three simulation runs per R1374/9A mutant and wild-type catch bond condition, respectively. The three simulation bond concentration and force outputs were time-averaged per condition.

RESULTS AND DISCUSSION

FN9-α_5 disengagement coincides with synergy site deactivation

We analyzed force-extension in conjunction with punctual stress to determine the role of the synergy site in FN9-α_5 disengagement. The initial force-extension curve of the wild-type $\alpha_5\beta_1$-FN structure followed a linear response for both 10 and 1 nm/ns pull rates until peaking at 729 and 462 pN, respectively (Fig. 2, *A* and *B*). The peak forces coincided with sharp decreases in the punctual stress at the synergy site, namely at sites R1374 and R1379 in FN9. R1379 has been shown to be connected to D154 in the α_5 head via a salt bridge (13). However, R1374 has not been previously observed to be actively linked to α_5. At both pull rates, R1374 retained higher punctual stresses than R1379, but the sequence of disengagement was dependent on the pull rate. Under the faster pull rate condition, the salt bridge was disrupted before a reduction in force on $\alpha_5\beta_1$-FN and punctual stress at R1374. This indicated that, while the load on FN was sufficient to overcome the energetic barrier to break the salt bridge connecting FN to α_5, persistent electrostatic interaction at R1374 enabled FN9 to remain near the α_5 head. This was not observed under the slower pull rate simulation, where we noted simultaneous punctual stress reduction in R1374 and R1379 at the peak force time point. While the punctual stresses at both residues were elevated during load ramping, synergy site engagement reduced after the force peak.

R1374 and R1379 were contributors to punctual stress at the synergy site before the drop in force on $\alpha_5\beta_1$-FN (Fig. S2). In both pull rate conditions, the combined punctual stress at R1374/9 before the force peak was on average two times higher than other synergy site residues. Due to the high electrostatic activity of both sites before FN9 and α_5 separation, we mutated both residues (R1374/9A) to evaluate their roles in maintaining $\alpha_5\beta_1$-FN's structural response to force. At 10 nm/ns, the force response of the wild-type and mutant $\alpha_5\beta_1$-FN were similar, peaking at 729 and 704 pN, respectively (Fig. 2 *C*). However, the punctual stresses at A1374 and A1379 were 45 and 40% lower in the mutant case than the wild-type (Fig. 2, *C* and *D*), indicating that the mutation disrupted synergy site engagement, but did not necessarily reduce force transmission. Similar trends were observed in the 1 nm/ns force rate condition, where the punctual stresses at A1374 and A1349 were small relative to R1374 and R1379, and the first peak force was lower in the mutant case (wild-type = 46 2pN, mutant = 291 pN; Fig. 2 *D*).

Although our results appeared to conflict with the understanding that synergy site mutagenesis decreases cell adhesion strength, the relative energetic barrier required to separate the synergy site from integrin revealed closer agreement with the literature (17,18,24,39,43). While we noticed a 171 pN difference (37% less than the wild-type) in the first peak force in the 1 nm/ns mutant model, we only noted a 25 pN drop (3% less than the wild-type) in the 10 nm/ns model. This is likely a consequence of the high pull rates used in these models that may hide molecular mechanisms. Therefore, long-term simulations at slower pull rates and smaller forces are needed to overcome this limiting factor. We worked toward this goal in a later

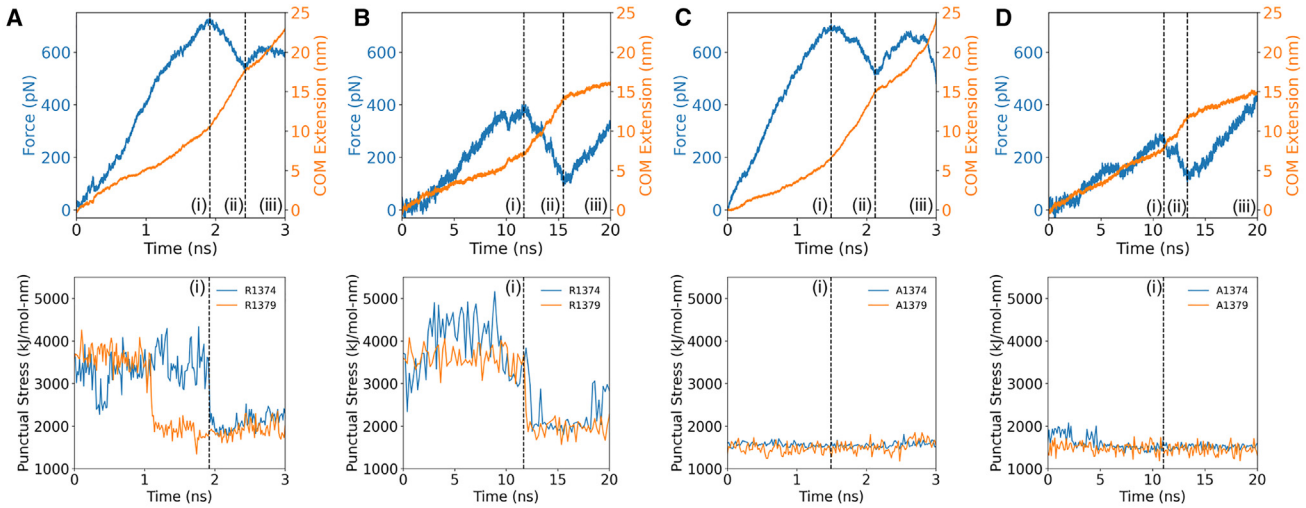

FIGURE 2 Force and COM extension over time plotted over punctual stress at R1374/1379 of the synergy site for (*A*) 10 nm/ns wild-type $\alpha_5\beta_1$-FN, (*B*) 1 nm/ns wild-type $\alpha_5\beta_1$-FN, (*C*) 10 nm/ns R1374/9A $\alpha_5\beta_1$-FN, and (*D*) 1 nm/ns R1374/9A $\alpha_5\beta_1$-FN. Positions (i), (ii), and (iii) correspond to the time at the peak force, local minimum, and final frame, respectively. To see this figure in color, go online.

section. For now, to overcome this potential conflict with the literature, we opted to use the area under the force-extension curve (Fig. S4) as a proxy for measuring synergy site departure energy, which would be related to the energy barrier required to pull FN9 away from α_5. We defined the *synergy site departure force* as point (i) in all simulations (Fig. 2). Forces recorded after the *synergy site departure force* would work to unfold FN and unbind RGD. We found that the synergy site departure energies were greater in the wild-type, in line with past in vitro experiments that show greater binding affinity of $\alpha_5\beta_1$ integrin to FN in the presence of the synergy site (24,39). At 10 nm/ns, the wild-type and mutant energies were 4012 and 2715 pN-nm, respectively. At 1 nm/ns, the wild-ype and mutant had energies of 1529 and 883 pN-nm, respectively. These values do not have any physical meaning, but enabled a comparison between the wild-type and mutant. From our current steered MD data, we cannot make claims about the effect of the synergy site on RGD binding specifically. Free energy methods such as free energy perturbation and molecular mechanics Poisson-Boltzmann surface area would be more appropriate to study these effects computationally and are the subject of ongoing work.

Punctual stress measurements provided insight into per-residue interactions at the synergy site and are substantiated by atomic-level interactions. Specifically, the formation and breakage of hydrogen bonds between α_5 and FN9 are essential for relaying force between the two. Since high punctual stresses were observed on R1374 and R1379, we tracked bonds between R1379-D154 and R1374-E124 (Fig. S5 *A*). At both pull rates, the R1379-D154 salt bridge was broken before the maximum force was reached, while residue R1374 remained bounded to either E124 or E81 depending on the pull rate (Fig. S5, *B* and *C*). The measured distance between R1374-E124 was within the range of a hydrogen bond (0.35 nm) after the departure of the R1379-D154 bond (10 nm/ns case; Fig. S5 *D*). At the slower pull rate, R1374 transitioned from E124 to E81, maintaining contact between FN9 and $\alpha_5\beta_1$ together with R1379-D154 (Fig. S5 *E*). Both bonds then released and the force on $\alpha_5\beta_1$-FN consequently dropped. The R1374/9A double mutation severed the main points of contact between FN9 and $\alpha_5\beta_1$, pushing the distance between the residues to 0.65 nm, beyond the 0.35 nm hydrogen bond length cutoff (Fig. S5 *F*).

For all test cases, the peak forces were followed by sharp increases in extension rate, suggesting a rapid conformational change of $\alpha_5\beta_1$-FN (Fig. 2). In the case of the wild-type 10 nm/ns pull rate, the measured extension rate increased from 5.10 to 14.4 nm/ns. Similarly, the wild-type 1 nm/ns pull rate increased in rate from 0.547 to 1.82 nm/ns (Table S4). Notably, there was a mismatch between the input rate and measured rate. Steered MD simulations attempt to control the pull rate via a virtual spring connecting a dummy atom to the pulled site. While the atom moves at a constant rate, the molecule's response depends on the virtual spring deflection and local conformational changes associated with the molecule. Therefore, it is unlikely that the input pull rate matches the measured pull rate experienced by the molecule. Furthermore, the output extension was measured as the distance traveled by $\alpha_5\beta_1$-FN's COM, which depends on the structural behavior.

Our reported forces and pull rates are many orders of magnitude higher than what has been tested using atomic force microscopy (AFM) (1–15 μm/s) (43). Given our large 1.5M atom system, we compromised on the simulation timescale by applying extension rates within the bounds of past steered MD simulations of integrin (0.1–10 nm/ns)

(22,44). The fast extension rates contributed to simulated forces beyond what has previously been measured experimentally (single-molecule rupture forces of 80–120 pN) (43). Nevertheless, the difference between the forces generated at 1 and 10 nm/ns hinted at force-dependent behavior arising from synergy site engagement. Larger conformational changes were visually noted in the α_5 head during 10 nm/ns pulling compared with 1 nm/ns pulling. Furthermore, the mutants showed little to no changes in the movement of the α_5 head, suggesting that the interactions at the synergy site could work to deform α_5. Therefore, we quantified the conformational changes associated with synergy site engagement when subjected to high pull rates.

Conformational response of α_5 and β_1 was hampered by lack of synergy site engagement

We informed the differences in force and extension rates across conditions by visualizing the structural changes of $\alpha_5\beta_1$-FN under both pull rates for the wild-type and mutant cases. We used the radius of gyration to quantify conformational changes within α_5 and β_1 heads, with smaller radii indicating more compact proteins. In both wild-type runs, the α_5 head, which is connected to the synergy site on FN9, stretched further than the β_1 head, which is connected to the RGD motif on FN10. However, pull rate affected the degree of α_5 stretching. The lower 1 nm/ns pull rate resulted in 0.165 nm increase in α_5's radius of gyration (Fig. 3 *A*) compared with a 0.407 nm increase in the 10 nm/ns rate simulation (Fig. S3 *A*). Most of the α_5 head deformation resulted before the peak force and synergy site disengagement. For the respective 10 and 1 nm/ns rates, 97.7 and 99.0% of the max α_5 head deformation occurred before the peak force, when the synergy site loosened. From the observations of $\alpha_5\beta_1$-FN's quaternary structure, we noticed the α_5 head straightening while FN9 remained connected at the synergy site (Fig. 3 *C*). Furthermore, at higher forces, α_5 underwent a greater degree of stretching while FN9 unfolded (Fig. S3 *C*). In contrast, lower forces seemed to encourage synergy site disengagement before FN unfolding. Our observation suggests that $\alpha_5\beta_1$-FN's catch bond dynamics may be promoted by greater synergy site interaction in combination with α_5 extension to resist larger forces. The greater interaction may stem from the hydrogen bond electrostatics at R1374 and R1379 that bridge α_5 to FN9 (Fig. S5).

We tested the degree to which the synergy site contributed to structural changes in $\alpha_5\beta_1$-FN by mutating the site (R1374/9A) and again measuring the radius of gyration of α_5 and β_1 under an external load on FN. Surprisingly, the mutant pulled at 10 nm/ns still resulted in conformational changes of the α_5 head, with the radius of gyration increasing by 0.266 nm. However, this was less than the 0.407 nm increase observed in the wild-type (Fig. S3 *B*). Furthermore, the mutant pulled at the slower 1 nm/ns showed virtually no deformation of α_5 or β_1 (Fig. 3 *B*). Investigating the quaternary structure of the mutant revealed that FN9 was separated immediately from α_5 (Figs. 3 *D* and S3 *D*). As the FN β sheets stacked vertically in alignment with the pulling direction, the force increased and peaked as soon as FN10 began to unfold. For all simulations, the β_1 head kept a more stable conformation, maintaining its radius of gyration within 0.12 nm. These results are indicative of a new mechanism whereby α_5 and FN deformation patterns may be altered due to interactions at the synergy site. However, the fast pull rates are five orders of magnitude higher than even the slowest AFM pull rates, posing the question of whether these states may be realized and, more importantly, have a physical meaning. So, while our results were promising, we aimed to address the pull rate limitation by conducting longer-term simulations and emphasizing our analysis on the synergy site and integrin interaction.

Synergy site interactions maintained FN9 and α_5 close

We used two 250 ns NPT simulations of $\alpha_5\beta_1$ integrin in complex with FN9-10 (wild-type and R1374/9A) to understand the role of the synergy site in maintaining integrin and FN conformational stability. Visual observation showed separation of mutant FN9 away from integrin as well as minor deviations to the integrin headpieces (Fig. 4 *B*). Therefore, we investigated the connection between FN9 and integrin. As expected, we found that the nonbonded interactions (van der Waals and Coulombic energies) between the synergy site and $\alpha_5\beta_1$ were greater in the wild-type structure (Fig. 4 *C*). These results aligned with the shorter distance between R1379 in FN9 and D154 in α_5 (Fig. 4 *D*) as well as the greater number of hydrogen bonds between the synergy site and α_5 (Fig. S6 *A*).

Lower synergy site engagement widened the gap between FN9 and α_5, but only minor structural changes in the integrin heads and FN were realized. We conducted structural analyses using the final 50 ns of the 250 ns simulation. The nonbonded interactions (Fig. 4 *A*), the hydrogen bond count (Fig. S6 *A*), and backbone RMSD (Fig. S6 *B*) of $\alpha_5\beta_1$-FN9-10 (wild-type and mutant) leveled off at $\approx$200 ns, suggesting system equilibration. Longer simulations would be necessary to evaluate whether the system fully equilibrated, but, based on these initial trends, we enforced the latter 50 ns cutoff. Since the synergy site in FN9 and RGD in FN10 are two anchoring contact points for integrin, we posited that releasing FN9 from α_5 via synergy site inhibition would increase FN9-10 flexibility. Interestingly, the means of the FN9-10 angles (θ_{FN}) in both cases was not statistically significant and variance was greater in the wild-type (Fig. 4 *E*), which would indicate that the wild-type FN9-10 was fluctuating to a greater degree even as the synergy site was interacting more strongly. Furthermore, the α_5-β_1 angle (θ_{int}) in the wild-type was 7.2° larger than the

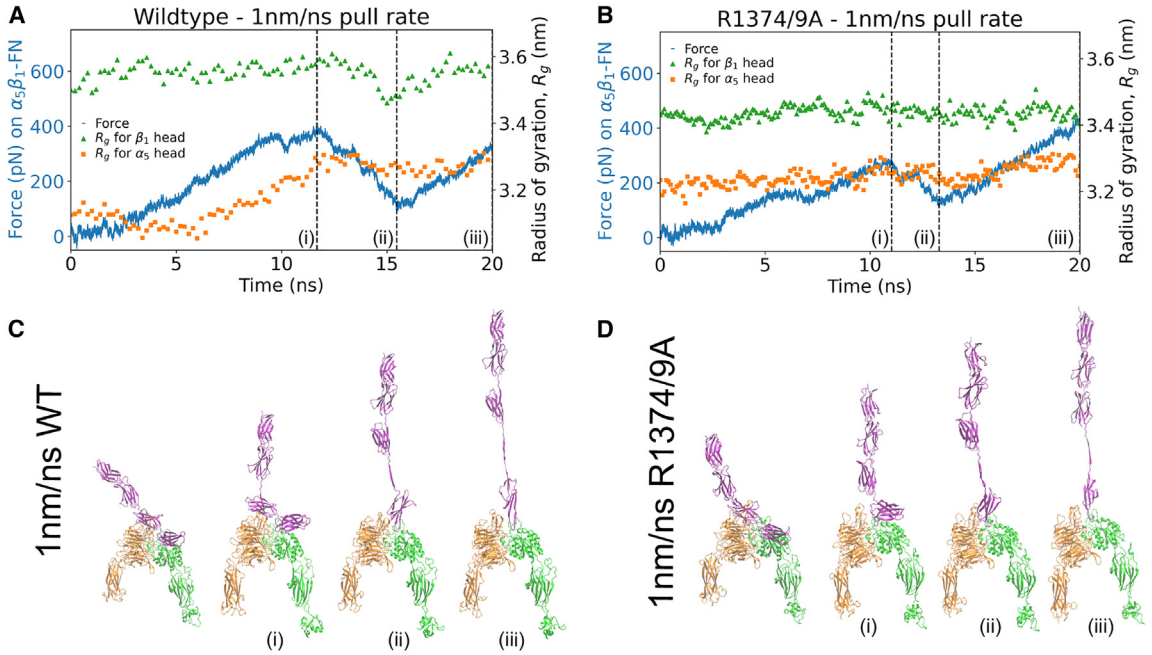

FIGURE 3 Force on $\alpha_5\beta_1$-FN and radius of gyration of α_5 and β_1 head for the 1 nm/ns runs for the (*A*) wild-type and (*B*) mutant. Positions (i), (ii), and (iii) correspond to the time at the peak force, local minimum, and final frame. The four shown frames from the simulation correspond to the first frame, (i) peak force, (ii) local minimum, and (iii) final frame for (*C*) wild-type and (*D*) mutant. To see this figure in color, go online.

mutant, pointing to a modest closing of the integrin heads in the mutant (Fig. 4 *F*). This closing was predominantly a result of FN9-10 rotation rather than a state transition of α_5. The propeller-thigh angle ($\theta_{\alpha 5}$) was 4.7° greater in the mutant, whereas the β_1-FN10 angle ($\theta_{\beta 1-FN10}$) was 12.1° lower in the mutant (Fig. S8). FN9-10 retained its shape, with only a 0.01 nm difference in radius of gyration between mutant and wild-type (Fig. S7, *A* and *B*). In addition, there was no statistically significant difference in the radius of gyration of α_5 between mutant and wild-type (Fig. S7, *C* and *D*). The radius of gyration of β_1 in the mutant was 0.16 nm smaller (Fig. S7, *E* and *F*), indicating a small amount of compression of β_1 as it interacted with FN10. The time series data of θ_{FN} (Fig. S6 *C*), θ_{int} (Fig. S6 *D*), $\theta_{\alpha 5}$ (Fig. S8 *B*), and $\theta_{\beta 1-FN10}$ (Fig. S8 *D*) showed overlap between mutant and wild-type throughout the entire simulation, meaning that some states may be similar to each other but, on average, the conformational measurements suggest that the synergy site locks FN9 to α_5 and prevents rotation of FN9-10.

The unlocking of FN9 due to reduced synergy site energetics did not promote appreciable changes at integrin's RGD binding location. We first measured the nonbonded interaction energies between RGD and $\alpha_5\beta_1$, including the MIDAS cation, which showed no differences in energies after, and even before the imposed 200 ns cutoff (Fig. S9 *A*). In addition, the number of hydrogen bonds between α_5 and RGD (Fig. S9 *B*) as well as β_1 and RGD (Fig. S9 *C*) were similar between the wild-type and mutant. From these data, we assumed that RGD would be a stable location for FN to maintain binding to integrin regardless of synergy site engagement. To confirm the conformational stability at the RGD binding area, we measured the mean and minimum distances between notable interactions at this site (Fig. S10 *A*). These included RGD-MIDAS (Fig. S10, *B* and *C*), D227-RGD (Fig. S10, *D* and *E*), and S134-MIDAS (Fig. S10, *F* and *G*). As expected, the distances between these pairs remained small in both the wild-type and mutant. Although there were differences in the S134-MIDAS mean and minimum distances, the observed 0.05–0.75 nm distance difference was not enough to decrease the absolute interaction energy at the mutant's RGD site (Fig. S9 *A*). The stability of the RGD binding site enabled it to behave like a pivot point for mutated FN9-10 when FN9 dislodged from the synergy site. Since our data suggest that RGD remained stable regardless of synergy site engagement, we reasoned that the additional synergy site interaction energies in the wild-type would only bolster $\alpha_5\beta_1$-FN binding. From past in vitro experiments, RGD alone is known to be sufficient to support some $\alpha_5\beta_1$ integrin binding and cell adhesion, although it has been shown that the synergy site promotes longer lasting binding and stronger cell adhesion when it binds in tandem with RGD to secure FN (6,24). The synergy site alone does not support cell adhesion as well as only RGD, or both RGD and the synergy site (45,46), which may be attributed to the synergy site's lower nonbonded interaction energy (Fig. 4 *C*) compared with RGD (Fig. S9 *A*). However, as mentioned, free energy methods must be considered to include the entropic effects that we do not account for in this work.

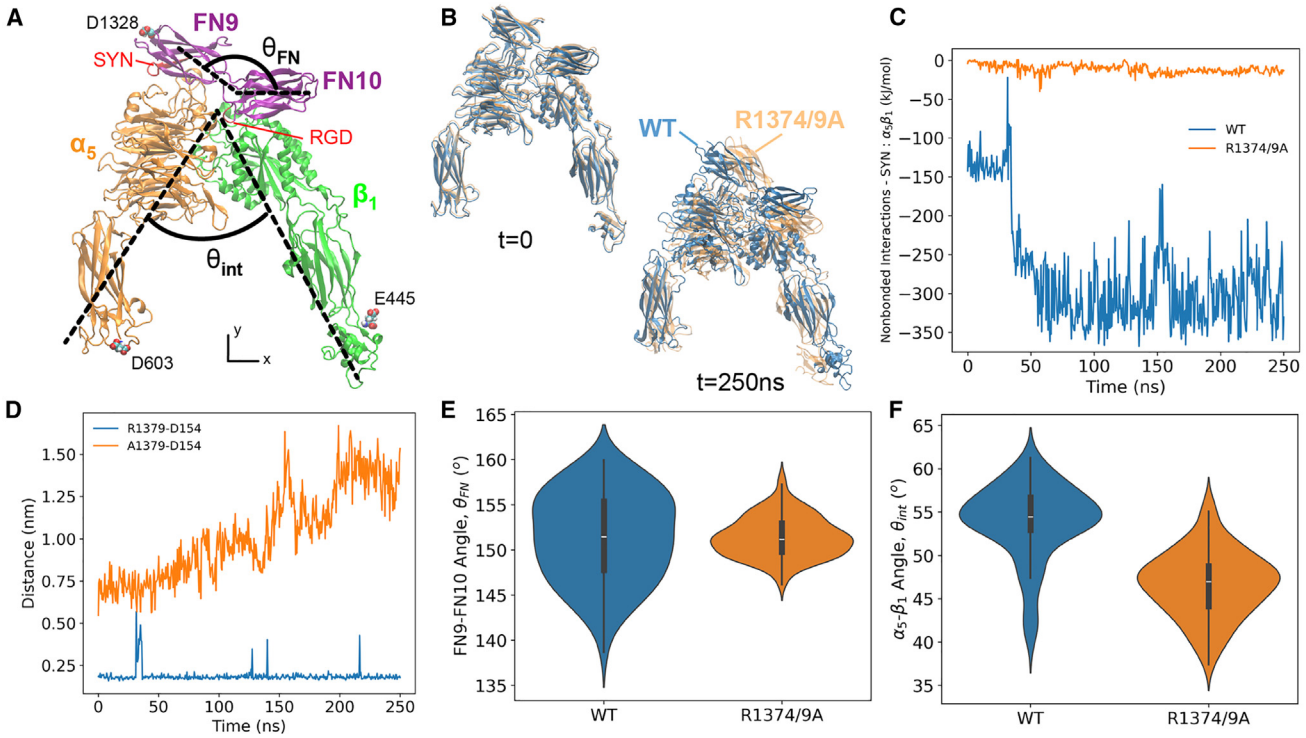

FIGURE 4 (*A*) Cryo-EM structure of $\alpha_5\beta_1$-FN9-10. Small restraints were placed on D603, E445, and D1348 in the *x* and *y* directions to mimic the respective continuing structures of integrin and FN. θ_{int} was defined the angle between the principal axes of inertia of α_5 and β_1, respectively. Similarly, θ_{FN} was defined as the angle between the principal axes of inertia of FN9 and FN10, respectively. Dashed lines are hand drawn and indicate an approximation of the principal axes. SYN, synergy site. (*B*) Superposition of the wild-type (*blue*) and mutant (*orange*) during the first and last frames of the respective 250 ns simulations. (*C*) Nonbounded interaction energy between the synergy site and $\alpha_5\beta_1$ integrin for wild-type and mutant. (*D*) Minimum distance between residue 1379 (FN9) and D154 (α_5) for wild-type and mutant. (*E*) Violin plot of FN9-10 angle for the last 50 ns of 250 ns simulation (WT $=$ $151.4\pm4.9^{\circ}$, R1374/9A $=$ $151.4\pm2.2^{\circ}$, $p = 0.98$). (*F*) Violin plot of $\alpha_5\beta_1$ angle for last 50 ns of 250 ns simulation (WT $=$ $53.9\pm4.3^{\circ}$, R1374/9A $=$ $46.7\pm3.8^{\circ}$, $p < 0.0001$). To see this figure in color, go online.

Collectively, our observations of the 250 ns NPT trajectories support the conjecture that the synergy site reinforces integrin engagement with the matrix (13,24). Furthermore, our accelerated steered MD models imply that force between the synergy site and α_5 integrin head may induce conformational changes of α_5 integrin. Overall, our results highlight the importance of the synergy site clip in stabilizing and reinforcing the $\alpha_5\beta_1$-FN bond after initial catch bond formation, which has also been previously suggested experimentally (9,25,47,48). While cell adhesion can be negated altogether by an RGD deletion as demonstrated by spinning disk assays, the R1374/9A double mutation reduces cell adhesion strength by around 90% (24). So, while adhesion could still occur, the bond strength was compromised due to the synergy site mutation, which has also been shown previously through single-molecule AFM (43). In addition, past surface plasmon resonance binding assays measure an 11-fold decrease in affinity between $\alpha_5\beta_1$ and R1374A FN compared wiith wild-type (39). Clearly, the role of the synergy site in maintaining a firm adhesion cannot be understated. Here, we propose how the synergy site may give rise to specific molecular states of $\alpha_5\beta_1$-FN, since it holds FN9 near α_5. Our steered MD models at a 1 nm/ns pull rate showed a decrease in initial synergy site departure energy after mutagenesis, implying that there is a greater energetic barrier in breaking the synergy site than when it is inhibited. Furthermore, the 1 nm/ns wild-type model predicts that the connection between FN9-α_5 maintained by the synergy site could deform the α_5 head when loaded, which was not observed in the 1 nm/ns mutant run. While our MD study highlighted the reinforcing role of the synergy site at the molecular scale, we also sought to explore how this adhesion reinforcement may dynamically manifest at the whole-cell scale.

Synergy site presence led to adhesion reinforcement by recruiting $\alpha_5\beta_1$ integrin

We employed a whole-cell FE model that analyzed the adhesion interface that contained $\alpha_5\beta_1$-FN bonds under an isotropic cell contraction that drove bond extension (Fig. 5 *A*). Our simple model demonstrated an adaptive reinforcement of collective $\alpha_5\beta_1$-FN bonds due to the stronger binding affinity afforded by the synergy site. We modified the parameters for the $\alpha_5\beta_1$-FN binding kinetics (Table S3) to produce bond lifetime curves for the wild-type bond and

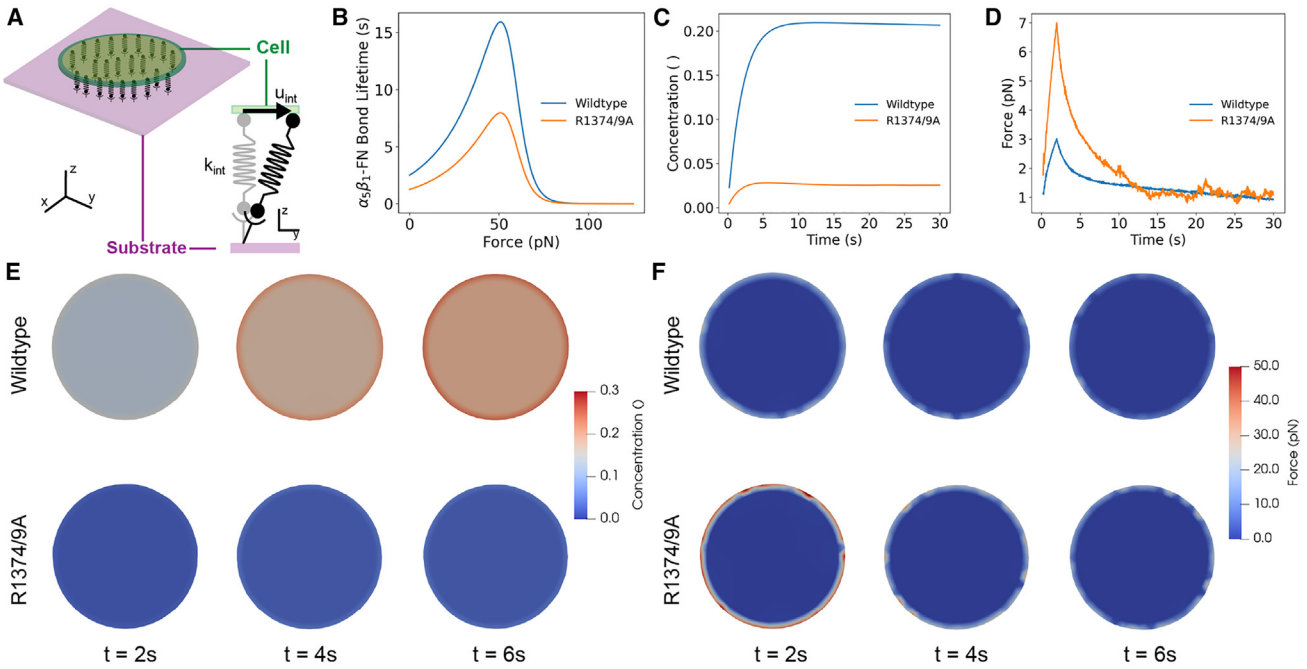

FIGURE 5 (*A*) Schematic of the whole-cell interface model that assumes that integrin behaves as a spring that is stretched due to cell contraction. (*B*) Catch bond model: $\alpha_5\beta_1$-FN bond lifetime versus applied force for wild-type (adapted from (38,39)). (*C*) Concentration over time of wild-type and mutant $\alpha_5\beta_1$-FN. (*D*) Force over time of wild-type and mutant $\alpha_5\beta_1$-FN. (*E*) Frames at times 2, 4, and 6 s indicating the concentration of $\alpha_5\beta_1$-FN bonds across the cell-substrate interface during a 200 Pa uniform contraction. (*F*) Frames at times 2, 4, and 6 s indicating the distribution of $\alpha_5\beta_1$-FN bond force across the cell-substrate interface during a 200 Pa uniform contraction. To see this figure in color, go online.

R1374/9A mutant (Fig. 5 *B*). The differences in parameters between the two bond types resulted in an 11-fold decrease in $\alpha_5\beta_1$-FN bond concentration (Fig. 5 *C*), but no increase in equilibrium force (Fig. 5 *D*). The areas of high concentrations and high forces are present at the periphery of the cell model during contraction (Fig. 5, *E* and *F*), which has been shown by 2D fluorescence resonance energy transfer and traction force microscopy assays (25). Notably, mutant bonds compensate for the lack of number of bonds by sustaining more of the cell's contractile load. The higher recruitment of wild-type bonds distributes the forces more evenly across the cell model.

Our whole-cell FE model sheds light on the dynamic force balance at short timescales that are not as apparent experimentally. Traction force microscopy of cells plated on 2D substrates have shown that cell contraction and individual bond force were not altered due to an absence of the synergy site (25,48). Our model used the same 200 Pa cell contraction across both conditions, but showed a stark difference in how the adhesion forces are handled by the bonds. Namely, while forces eventually equalized between mutant and wild-type conditions, we observed an initial dynamic adjustment of high forces at the cell model's boundary for mutant bonds (Fig. 5 *F*). Specifically, average forces measured from mutated bonds peaked at 7 pN, while wild-type bonds peaked at 3 pN; both average bond forces were within the previously measured 1–7 pN range (25). A body of work has shown the reduction in cell adhesion strength at the single-molecule and whole-cell scale due to a lack of synergy site engagement (24,25,43,48). Despite the reduced bond strength, our model showed that, under minimal tension, the binding affinity gain due to the presence of the synergy led to a more stable, dynamic force balance across the $\alpha_5\beta_1$-FN bonds on the cell model's surface.

Pivot-clip mechanism of $\alpha_5\beta_1$-FN as a model for cell adhesion reinforcement

The mechanosensitive pivot-clip mechanism provides a model to consider how the $\alpha_5\beta_1$-FN catch bond reinforces cell adhesion across molecular and cell scales under cell-matrix forces (Fig. 6). Long-term NPT simulations indicated that role of the synergy site was to clip FN9 close to α_5 as demonstrated by the increased separation between FN9 and α_5 in the mutant. The dislodging of FN9 did not modify the stability of the RGD site. In our steered MD simulations, for both pull rates tested in the wild-type $\alpha_5\beta_1$-FN, the unbinding of FN9-α_5 coincided with a plateauing of α_5 extension (Figs. 3 *A* and S3 *A*). With the link between FN9-α_5 broken, FN10 was free to rotate about the RGD motif on β_1 (Figs. 3 *D* and S3 *D*). The FN10 rotation about the RGD site was maintained in the mutant steered MD runs while diminishing the increase in radius of gyration of α_5 (Fig. S3, *B* and *D*). Based on the structural changes observed on α_5 in the steered MD simulations, the synergy site clipped the α_5 head to FN9 while the RGD motif on β_1 acted as a pivot

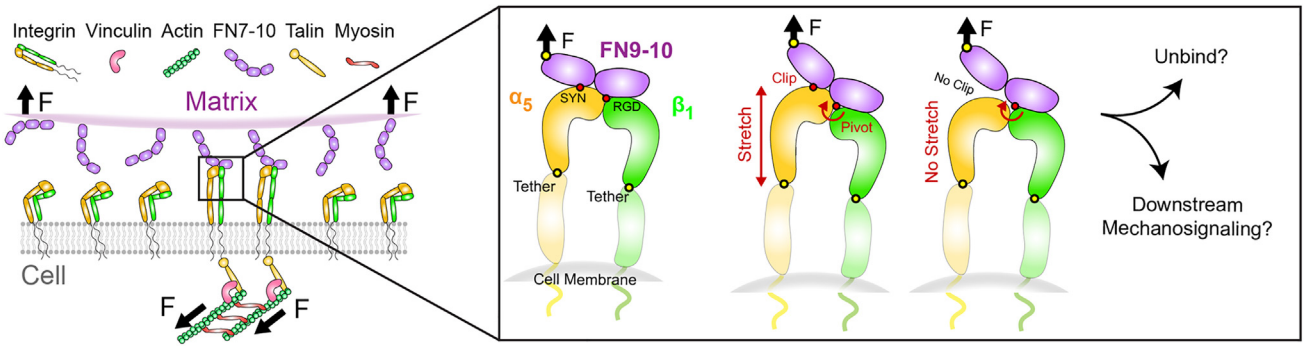

FIGURE 6 Proposed model for synergy site clip engagement leading to α_5 deformation during mechanosensing while RGD acts as a pivot for FN10. In this model, force transmits across the clip, stretching α_5. The additional energetic barrier provided by the clip could afford $\alpha_5\beta_1$-FN greater resistance to unbinding. The rigidity of β_1 relative to α_5 may allow for force transmission across the membrane and toward the mechanosensitive cytoskeletal protein, talin, leading to downstream mechanosignaling. To see this figure in color, go online.

for FN10 (Fig. 6). Since α_5 preferentially stretched instead of β_1, we conducted 100 ns NPT simulations of each integrin head to measure each of their relative extensional stiffness. Upon confirming a stable RMSD after 50 ns (Fig. S11 *A*), we averaged the measured α_5 and β_1 head distances over five 10 ns blocks (Fig. S11 *B*) to quantify extensional stiffness. We measured extensional stiffnesses of 2587 and 174,548 pN/μm for the α_5 and β_1 heads, respectively (Fig. S11 *C*). Based on the distance fluctuations, β_1 remained more static, while α_5 seemed to oscillate. We also found that the propeller-thigh angle of α_5 decreased (Fig. S11 *D*), giving α_5 a more bent shape (Fig. S11 *E*). We reasoned that the link between the propeller and thigh grants α_5 its flexibility to stretch when force is applied, while β_1's rigidity could provide a route for forces to transmit toward cytoskeletal proteins. While it has been known that the synergy site plays a role in catch bond dynamics (17,24), the clip engagement under force could be one mechanism by which the synergy site enables catch bond dynamics at the molecular scale. Using our pivot-clip model (Fig. 6), forces generated at the cell-matrix interface would need to first overcome the synergy site clip energy barrier. In parallel, α_5 would resist forces by stretching before FN9 unclipping, also leading to a higher barrier than if the synergy site were not present. In addition, the rigidity of β_1 could facilitate downstream mechanosignaling via talin. Namely, talin binds to the β_1 tail and has been shown to be a mechanosensitive protein that interacts with vinculin and focal adhesion kinase to promote focal adhesion maturation and nuclear localization of transcriptional coregulator, yes-associated protein (49,50,36). However, larger forces could also increase the probability of FN unbinding from $\alpha_5\beta_1$, especially when the additional energetic barrier from the synergy site is not present. Past assays have demonstrated that $\alpha_5\beta_1$-FN unbinding occurs with greater likelihood when the synergy site is inhibited; moreover, $\alpha_5\beta_1$-FN loses its catch bond characteristics (18,24). To determine the exact pathway of the force transmission across the $\alpha_5\beta_1$-FN catch bond with and without the synergy site, much longer and slower MD simulations are needed. Along those lines, more investigation is warranted to elucidate how the full structure of $\alpha_5\beta_1$ dynamically couples with mechanosensitive cytoskeletal proteins at the atomistic scale.

In the context of outside-in signaling, the $\alpha_5\beta_1$-FN pivot-clip mechanism demonstrates how the synergy site could route force via β_1 toward mechanosignaling proteins in the cytoplasm, like talin, leading to integrin clustering. According to the outside-in activation model, integrins maintain a bent-closed, low-affinity state before undergoing a conformational change to an extended, active conformation upon encountering an ECM ligand (Fig. 1 *A*) (51–53). In contrast, the inside-out model proposes that the adaptor protein talin would bind to the cytoplasmic tail of integrin, allowing it to activate and subsequently bind to its ligand (51–53). While the current hypothesis states that binding between FN and $\alpha_5\beta_1$ triggers an opening of integrin's cytoplasmic tails leading to an accumulation of adaptor proteins that resist cell-matrix forces (Fig. 6), further studies are needed to elucidate the mechanism behind integrin activation. Multiple steered MD models have been employed to interrogate β_3 integrin activation (22,44,54–57), with few investigating the cytoplasmic end of β integrin (58–60). However, to our knowledge, our approach is unique in that we model the interface between FN and the $\alpha_5\beta_1$ integrin heads, where forces are transmitted bidirectionally between the cell and its matrix.

Our study acknowledges several limitations. Firstly, we made the assumption that the proximal ends of the integrin heads were anchored by fully extended integrin legs tightly held by tails in the cell membrane. While this assumption contributed to model stability, it is worth noting that the head-leg junction has been suggested to possess greater flexibility (13). Relaxing the constraints on the proximal ends to allow lateral movement may introduce flexibility without the added complexity of integrating the legs. Secondly, our steered MD models applied a large, vertical pulling rate. While this approach is advantageous for directly stressing the points of contact between FN and $\alpha_5\beta_1$, it could

introduce biased pulling and rotational forces that are unrealistic, which would decrease model confidence. Multiple runs and a parametric study of boundary conditions must be considered when confirming our MD simulations in future works investigating tension or other loading modalities, such as shear or torsion. Finally, our focus was on a specific integrin subtype. The intricate nature of cell-matrix interactions involves multiple integrin subtypes and their respective ligands. Due to the prohibitive cost of MD simulations, alternative approaches such as coarse-grained or agent-based models, capable of examining cell-matrix interactions at a broader systems level and over extended timescales, may be necessary.

CONCLUSION

This work advances our understanding of cell mechanobiology by introducing a mechanosensitive mechanism, termed pivot-clip, by which $\alpha_5\beta_1$ integrin reinforces cell adhesion. Using FE and MD simulations, we shed light on a biophysical connection between the cell and ECM that underpins many cellular behaviors that drive physiology and pathology. Critically, we also demonstrated binding domains that promote catch bond dynamics in the context of cell-matrix mechanosensing. Looking forward, we envision elucidating how the force-dependent, pivot-clip mechanism interacts with its surrounding machinery and how it may be transformed via novel therapeutics. As our understanding of cell adhesion progresses, we aim to develop informed approaches to target diseases that rely on transmitting forces via cell-matrix bonds.

SUPPORTING MATERIAL

Supporting material can be found online at https://doi.org/10.1016/j.bpj.2024.06.008.

AUTHOR CONTRIBUTIONS

A.R.M., A.B.T., and M.R.K.M. conceptualized and designed the research. A.R.M., A.B., and W.W. performed the research and analyzed data. A.R.M. wrote the manuscript. G.D.O., A.B.T., and M.R.K.M. supervised the research and edited the manuscript.

ACKNOWLEDGMENTS

This research used the Expanse at San Diego Supercomputer Center through allocation MCB100146 from the Advanced Cyberinfrastructure Coordination Ecosystem: Services & Support (ACCESS) supercomputing facilities, supported by the National Science Foundation (NSF) (grant nos. 2138259, 2138286, 2138307, 2137603, and 2138296). We also acknowledge the additional allocation, BIO230214 for use of Expanse as well as the Negishi Community Cluster managed by the Rosen Center for Advanced Computing. A.R.M. was supported by the Ford Predoctoral Fellowship, UC Berkeley College of Engineering Robert N. Noyce Fellowship, and Hearts to Humanity Eternal Research Fellowship. A.B. was supported by the National Institute of Health Maximizing Access to Research Careers T34 Award. W.W. was supported by the NSF Research Experience for Undergraduates via the Transfer-to-Excellence Program at University of California, Berkeley. A.B.T. was supported by the UC Berkeley Miller Institute for Basic Research in Science. We thank members of the Molecular Cell Biomechanics and Berkeley Biomechanics Labs for fruitful discussions that led to the improvement of the manuscript. Special thank you to Mohammad Khavani for his suggestions to improve the molecular dynamics simulations.

DECLARATION OF INTERESTS

The authors declare no competing interests.

REFERENCES

1. Damiano, J. S., A. E. Cress, …, W. S. Dalton. 1999. Cell adhesion mediated drug resistance (CAM-DR): role of integrins and resistance to apoptosis in human myeloma cell lines. *Blood.* 93:1658–1667.
2. Bachmann, M., S. Kukkurainen, …, B. Wehrle-Haller. 2019. Cell adhesion by integrins. *Physiol. Rev.* 99:1655–1699.
3. Lee, M. H., P. Ducheyne, …, R. J. Composto. 2006. Effect of biomaterial surface properties on fibronectin–$\alpha5\beta1$ integrin interaction and cellular attachment. *Biomaterials.* 27:1907–1916.
4. Hynes, R. O. 2002. Integrins: bidirectional, allosteric signaling machines. *Cell.* 110:673–687.
5. Shams, H., B. D. Hoffman, and M. R. K. Mofrad. 2018. The "stressful" life of cell adhesion molecules: on the mechanosensitivity of integrin adhesome. *J. Biomech. Eng.* 140:020807.
6. Cutler, S. M., and A. J. García. 2003. Engineering cell adhesive surfaces that direct integrin $\alpha5\beta1$ binding using a recombinant fragment of fibronectin. *Biomaterials.* 24:1759–1770.
7. Scheiblin, D. A., J. Gao, …, M. K. Duncan. 2014. Beta-1 integrin is important for the structural maintenance and homeostasis of differentiating fiber cells. *Int. J. Biochem. Cell Biol.* 50:132–145.
8. Humphrey, J. D., E. R. Dufresne, and M. A. Schwartz. 2014. Mechanotransduction and extracellular matrix homeostasis. *Nat. Rev. Mol. Cell Biol.* 15:802–812.
9. Benito-Jardón, M., S. Klapproth, …, M. Costell. 2017. The fibronectin synergy site re-enforces cell adhesion and mediates a crosstalk between integrin classes. *Elife.* 6:e22264.
10. Hou, J., D. Yan, …, H. Cui. 2020. The roles of integrin $\alpha5\beta1$ in human cancer. *OncoTargets Ther.* 13:13329–13344.
11. Zhao, X.-K., Y. Cheng, …, Q. Zhang. 2016. Focal adhesion kinase regulates fibroblast migration via integrin beta-1 and plays a central role in fibrosis. *Sci. Rep.* 6:19276.
12. Cao, L., J. Nicosia, …, T. H. Barker. 2017. Detection of an integrin-binding mechanoswitch within fibronectin during tissue formation and fibrosis. *ACS Nano.* 11:7110–7117.
13. Schumacher, S., D. Dedden, …, N. Mizuno. 2021. Structural insights into integrin $\alpha5\beta1$ opening by fibronectin ligand. *Sci. Adv.* 7:eabe9716.
14. Kechagia, J. Z., J. Ivaska, and P. Roca-Cusachs. 2019. Integrins as biomechanical sensors of the microenvironment. *Nat. Rev. Mol. Cell Biol.* 20:457–473.
15. Schaffner, F., A. M. Ray, and M. Dontenwill. 2013. Integrin $\alpha5\beta1$, the fibronectin receptor, as a pertinent therapeutic target in solid tumors. *Cancers.* 5:27–47.
16. Cox, D., M. Brennan, and N. Moran. 2010. Integrins as therapeutic targets: lessons and opportunities. *Nat. Rev. Drug Discov.* 9:804–820.
17. Kong, F., A. J. García, …, C. Zhu. 2009. Demonstration of catch bonds between an integrin and its ligand. *J. Cell Biol.* 185:1275–1284.
18. Strohmeyer, N., M. Bharadwaj, …, D. J. Müller. 2017. Fibronectin-bound $\alpha5\beta1$ integrins sense load and signal to reinforce adhesion in less than a second. *Nat. Mater.* 16:1262–1270.

19. Dansuk, K. C., and S. Keten. 2021. Self-strengthening biphasic nanoparticle assemblies with intrinsic catch bonds. *Nat. Commun.* 12:85.
20. Dansuk, K. C., S. Pal, and S. Keten. 2023. A catch bond mechanism with looped adhesive tethers for self-strengthening materials. *Commun. Mater.* 4:60.
21. Yuan, Z., X. Duan, …, J. Huang. 2023. Catch bond-inspired hydrogels with repeatable and loading rate-sensitive specific adhesion. *Bioact. Mater.* 21:566–575.
22. Kulke, M., and W. Langel. 2020. Molecular dynamics simulations to the bidirectional adhesion signaling pathway of integrin $\alpha V\beta 3$. *Proteins.* 88:679–688.
23. Montes, A. R., G. Gutierrez, …, M. R. K. Mofrad. 2023. Multiscale computational framework to investigate integrin mechanosensing and cell adhesion. *J. Appl. Phys.* 134:114702.
24. Friedland, J. C., M. H. Lee, and D. Boettiger. 2009. Mechanically activated integrin switch controls $\alpha 5\beta 1$ function. *Science.* 323:642–644.
25. Chang, A. C., A. H. Mekhdjian, …, A. R. Dunn. 2016. Single molecule force measurements in living cells reveal a minimally tensioned integrin state. *ACS Nano.* 10:10745–10752.
26. Abraham, M. J., T. Murtola, …, E. Lindahl. 2015. GROMACS: High performance molecular simulations through multi-level parallelism from laptops to supercomputers. *SoftwareX.* 1–2:19–25.
27. Schrödinger, L. 2015. The PyMOL Molecular Graphics System, Version 1.8.
28. Webb, B., and A. Sali. 2016. Comparative protein structure modeling using MODELLER. *Curr. Protoc. Bioinformatics.* 54:5–6.
29. Humphrey, W., A. Dalke, and K. Schulten. 1996. VMD: visual molecular dynamics. *J. Mol. Graph.* 14:33.
30. Costescu, B. I., and F. Gräter. 2013. Time-resolved force distribution analysis. *BMC Biophys.* 6:1–5.
31. Tong, D., N. Soley, …, T. C. Bidone. 2023. Integrin αIIb$\beta 3$ intermediates: From molecular dynamics to adhesion assembly. *Biophys. J.* 122:533–543.
32. Luo, Q., D. Kuang, …, G. Song. 2016. Cell stiffness determined by atomic force microscopy and its correlation with cell motility. *Biochim. Biophys. Acta.* 1860:1953–1960.
33. Schierbaum, N., J. Rheinlaender, and T. E. Schäffer. 2019. Combined atomic force microscopy (AFM) and traction force microscopy (TFM) reveals a correlation between viscoelastic material properties and contractile prestress of living cells. *Soft Matter.* 15:1721–1729.
34. Chen, C., J. Xie, …, L. Yang. 2014. Substrate stiffness together with soluble factors affects chondrocyte mechanoresponses. *ACS Appl. Mater. Interfaces.* 6:16106–16116.
35. Guo, Y., S. Calve, and A. B. Tepole. 2022. Multiscale mechanobiology: Coupling models of adhesion kinetics and nonlinear tissue mechanics. *Biophys. J.* 121:525–539.
36. Cheng, B., W. Wan, …, M. Lin. 2020. Nanoscale integrin cluster dynamics controls cellular mechanosensing via FAKY397 phosphorylation. *Sci. Adv.* 6:eaax1909.
37. Bell, G. I. 1978. Models for the specific adhesion of cells to cells: a theoretical framework for adhesion mediated by reversible bonds between cell surface molecules. *Science.* 200:618–627.
38. Bidone, T. C., A. V. Skeeters, …, G. A. Voth. 2019. Multiscale model of integrin adhesion assembly. *PLoS Comput. Biol.* 15:e1007077.
39. Takagi, J., K. Strokovich, …, T. Walz. 2003. Structure of integrin $\alpha 5\beta 1$ in complex with fibronectin. *EMBO J.* 22:4607–4615.
40. Gaudet, C., W. A. Marganski, …, J. Y. Wong. 2003. Influence of type I collagen surface density on fibroblast spreading, motility, and contractility. *Biophys. J.* 85:3329–3335.
41. Neurohr, G. E., and A. Amon. 2020. Relevance and regulation of cell density. *Trends Cell Biol.* 30:213–225.
42. Brochu, T., and R. Bridson. 2009. Robust topological operations for dynamic explicit surfaces. *SIAM J. Sci. Comput.* 31:2472–2493.
43. Li, F., S. D. Redick, …, V. T. Moy. 2003. Force measurements of the $\alpha 5\beta 1$ integrin–fibronectin interaction. *Biophys. J.* 84:1252–1262.
44. Chen, W., J. Lou, …, C. Zhu. 2011. Molecular dynamics simulations of forced unbending of integrin $\alpha V\beta 3$. *PLoS Comput. Biol.* 7:e1001086.
45. Aota, S., M. Nomizu, and K. M. Yamada. 1994. The short amino acid sequence Pro-His-Ser-Arg-Asn in human fibronectin enhances cell-adhesive function. *J. Biol. Chem.* 269:24756–24761.
46. Redick, S. D., D. L. Settles, …, H. P. Erickson. 2000. Defining fibronectin's cell adhesion synergy site by site-directed mutagenesis. *J. Cell Biol.* 149:521–527.
47. García, A. J., J. E. Schwarzbauer, and D. Boettiger. 2002. Distinct activation states of $\alpha 5\beta 1$ integrin show differential binding to RGD and synergy domains of fibronectin. *Biochemistry.* 41:9063–9069.
48. Tan, S. J., A. C. Chang, …, A. R. Dunn. 2020. Regulation and dynamics of force transmission at individual cell-matrix adhesion bonds. *Sci. Adv.* 6:eaax0317.
49. Zhou, D. W., M. A. Fernández-Yagüe, …, A. J. García. 2021. Force-FAK signaling coupling at individual focal adhesions coordinates mechanosensing and microtissue repair. *Nat. Commun.* 12:2359.
50. Holland, E. N., M. A. Fernández-Yagüe, …, A. J. García. 2024. FAK, vinculin, and talin control mechanosensitive YAP nuclear localization. *Biomaterials.* 308:122542.
51. Jahed, Z., H. Shams, …, M. R. K. Mofrad. 2014. Mechanotransduction pathways linking the extracellular matrix to the nucleus. *Int. Rev. Cell Mol. Biol.* 310:171–220.
52. Shattil, S. J., C. Kim, and M. H. Ginsberg. 2010. The final steps of integrin activation: the end game. *Nat. Rev. Mol. Cell Biol.* 11:288–300.
53. Takagi, J., B. M. Petre, …, T. A. Springer. 2002. Global conformational rearrangements in integrin extracellular domains in outside-in and inside-out signaling. *Cell.* 110:599–611.
54. Jamali, Y., T. Jamali, and M. R. K. Mofrad. 2013. An agent based model of integrin clustering: exploring the role of ligand clustering, integrin homo-oligomerization, integrin–ligand affinity, membrane crowdedness and ligand mobility. *J. Comput. Phys.* 244:264–278.
55. Mehrbod, M., S. Trisno, and M. R. K. Mofrad. 2013. On the activation of integrin αIIb$\beta 3$: outside-in and inside-out pathways. *Biophys. J.* 105:1304–1315.
56. Su, S., Y. Ling, …, J. Wu. 2022. Force-enhanced biophysical connectivity of platelet $\beta 3$ integrin signaling through Talin is predicted by steered molecular dynamics simulations. *Sci. Rep.* 12:4605.
57. Shams, H., and M. R. K. Mofrad. 2017. α-Actinin induces a kink in the transmembrane domain of β3-integrin and impairs activation via talin. *Biophys. J.* 113:948–956.
58. Ji, Y., Y. Fang, and J. Wu. 2022. Tension Enhances the Binding Affinity of $\beta 1$ Integrin by Clamping Talin Tightly: An Insight from Steered Molecular Dynamics Simulations. *J. Chem. Inf. Model.* 62:5688–5698.
59. Pan, D., and Y. Song. 2010. Role of altered sialylation of the I-like domain of $\beta 1$ integrin in the binding of fibronectin to $\beta 1$ integrin: thermodynamics and conformational analyses. *Biophys. J.* 99:208–217.
60. Haydari, Z., H. Shams, …, M. R. K. Mofrad. 2020. Kindlin assists talin to promote integrin activation. *Biophys. J.* 118:1977–1991.